Chalcogenide Letters Vol. 22, No. 9, September 2025, p. 829 - 845

The GGA-mBJ analysis of Ni modified SrS alloys for magnetic ordering and energy harvesting applications

I. Sajjad [a], U. Parveen, H. Al-Ghamdi [b,*], M. Yaseen [a], S. Saleem [a], Nasarullah [a]
[a] *Spin-Optoelectronics and Ferro-Thermoelectric (SOFT) Materials and Devices Laboratory, Department of Physics, University of Agriculture, Faisalabad 38040, Pakistan*
[b] *Department of Physics, College of Sciences, Princess Nourah bint Abdulrahman University, P. O. Box 84428, Riyadh 11671, Saudi Arabia*

Herein, we employed modified Becke-Johson (mBJ) potential based first principles method to investigate the structural, optoelectronic, and magnetic properties of pure SrS and Ni doped $Sr_{1-x}Ni_xS$ alloys at varying doping concentrations. Formation enthalpy analysis predicts thermodynamical stability of resultant alloys. Geometry optimization was performed in order to optimize the super cells to obtain ground state energy state. After confirming their stability, we investigated their magnetic, electronic, and optical attributes. Pure SrS exhibits an indirect band gap of 3.53 eV (which is in good agreement with experiments), while nickel doping in SrS results in lowering the bandgap to the range of visible light absorption. Ni doping also causes the induction of magnetic moment in crystal lattice, transforming the resultant alloys into dilute magnetic semiconductors. The density of state (DOS) analysis revealed that d orbital of dopant Ni is mainly responsible for this magnetic semiconducting character. The magnetization accounts for 2.0 μ_B (6.25% lightly doped Ni-SrS) up to ~8.0 μ_B (25% densely doped Ni-SrS). We report ample amount of absorbance of visible light for Ni-SrS systems, which is encouraging for future prospects. Moreover, for thermoelectric device applications, the figure of merit (ZT~0.75) plots for densely (25%) Ni doped SrS show higher values at elevated temperatures. Overall, results suggest that $Sr_{1-x}Ni_xS$ alloys are promising candidate for applications in the field of thermoelectric generators, optical absorbers, solar cells, and spintronic devices.

(Received June 20, 2025; Accepted September 23, 2025)

Keywords: First principles, Ni doped SrS, Optoelectronics, Spintronics, FP-LAPW, Wien2k, Binary compounds

1. Introduction

Diluted magnetic semiconductors are designed by incorporation of transition metal elements in pure semiconductor matrix [7-10]. It is an interesting fact that dopant element does not disrupt their traditional semiconducting behavior but merely induces magnetism in host non-magnetic semiconductor material, however, we need to be precise about doping concentration, selection of dopant element and host materials ability to efficiently incorporate substitutional atoms [11, 12]. For practical applications like, magnetic based sensors, light emitting diodes, spin valves, logical devices and ultrafast optical switching, maintaining a particular magnetic ordering at elevated temperatures has more significance, threshold of which is commonly termed as Curie temperature (T_C) [13]. Various researchers reported high (T_c) ferromagnetism in transition metal doped binary systems such as ~5% Mn doped GaN, ~10% Mn doped ScN and $Ca_{0.75}TM_{0.25}S$ (TM=Mn, Ni and Co) [14-16]. Experimentally, more DMSs [17-22] have been explored applicable for proficient devices such as ultra-fast memory chips, ultra smart diodes, spin dependent transistors and spin-based valves [23].

In this regard, alkaline earth chalcogenides (II-VI) are the family of materials known for their simple structure which is beneficial for engineering, finding extensive applications in solar cells, optoelectronics, ion exchange, high carrier mobility, and photocatalysis [24-26]. Particular

* Corresponding author: hmalghmdi@pnu.edu.sa
https://doi.org/10.15251/CL.2025.229.829

case is SrS, which is recognized for its modest band gap (E_g), stable structure, low-cost synthesis, and positive temperature coefficient, make it a potential material for optoelectronic and thermoelectric (TE) usages, and various gas sensing instruments [27-29]. However, despite its stability along with cost effectiveness, SrS lacks magnetism, which restricts its possible applications in spintronics. One way to modify these properties is the substitutionally alloying the SrS with transition metals, enabling its use in practical applications [30]. For instance, it has been reported that $Sr_{0.75}Ti_{0.25}S$ and $Sr_{0.875}Ti_{0.125}S$ alloys exhibit half-metallic ferromagnetism (HMF), highlighting their potential for spintronic devices [31]. Labidi et al. reported significant modifications in the $Pb_{1-x}Sr_xS$ alloy system and identified its potential for optical usages, as the E_g transitions from indirect E_g to direct at x = 0.82 [32]. Gao et al. investigated various alkaline earth metal carbides with a zinc-blende structure and observed that AeC (Ae = Ba, Sr, Ca) exhibit HMF behavior, with E_g values of 2.01/2.48/3.25 eV, respectively, in the majority spin [33]. Yari et al. showed that 12.5% Cr doping in SrS converted it from a semiconductor to a half-metal with full spin polarization and induced counterclockwise polarization of reflected light in the ultraviolet spectrum [34]. Another study probed the role of Ba incorporation on the physical properties of SrS and predicted the potential of resultant ternary alloys for applications in optoelectronics and luminescent devices [35].

SrS shows potential for exploring the effects of magnetic cations on its physical properties, which could lead to significant advancements in condensed matter physics [36-38]. This study investigates $Sr_{1-x}Ni_xS$ (x = 6.25%, 12.5%, and 25%) alloys to better understand how varying Ni concentrations influence the material's properties. Herein, we report that Ni doping induces spin splitting across the Fermi level (F_E), primarily driven by the Ni dopant with a magnetic moment of 1.3 μ_B per unit cell. This strong magnetic ordering could stimulate experimental spintronics researchers to explore these doped alloys for potential usages in spin-based optical devices.

2. Computational methods

DFT based computations were employed to investigate the electronic, structural, and optical characteristics of $Sr_{1-x}Ni_xS$ alloys. The FP-LAPW approach within the WIEN2K code was utilized for computational analysis [39, 40]. It provides the eigen functions and eigen values of the Kohn-Sham (KS) equations [41, 42]. In this technique, the unit cell is split into an interstitial region (IR) and atomic spheres (muffin-tin MT). The muffin tin radii (R_{MT}) value for Ni, Sr, and S are 2.10, 2.10 and 2.18 a.u., correspondingly. The potential in two stated regions was calculated using the following equation [43, 44]

$$V(r) = \begin{cases} \sum_{LM} V_{LM}(r) Y_{LM}(\hat{r}) & \dots\dots\dots\dots\ (i) \\ \sum_K V_K e^{iK.r} & \dots\dots\dots\dots\ (ii) \end{cases} \quad (1)$$

For the self-consistent field computations, modified Becke-Jonson (mBJ) potential was used [45]. For the computation of valence shell electronic states, focus was directed on the partially filled states: [Kr] $5s^2$ for Sr, [Ne] $3s^2$ $3p^4$ for S, and [Ar] $3d^8$ $4s^2$ for Ni. The G_{max} and l_{max} parameters corresponding values were set as 16 and 10. The parameter $R_{MT} \times K_{max} = 8$ was set in order to adjust the expansion of wave functions. Here, R_{MT} is the radius of smallest sphere under consideration while the K_{max} parameter is the wave vector's cut-off value. Optimized lattice constants were obtained via geometry optimization. In the process, atomic positions were also relaxed till the atomic forces between atoms reached < 0.1 mRy for each atom. The self-consistent iteration convergence was achieved with a total energy less than 10^{-2} mRy. A 1000 k-point mesh was selected inside the irreducible Brillouin zone (BZ). Additionally, dielectric constant was computed by employing Kramers-Krong relation and particular equations were implemented to investigate the related optical parameters [46, 47].

3. Results and discussion

3.1. Structural properties

Any materials applications in practical fields are directly dependent on the its stability under various conditions. In our stability analysis, we provide stability evidence of resultant Ni-SrS alloys in by computing three different parameters termed as: (i) structural stability, (ii) magnetic ordering, and (iii) thermodynamical stability. Structural stability analysis of a material provides in-depth insight about ground state parameters [48]. The pristine SrS crystalizes in a rock salt lattice under standard conditions [49], where Sr lies at 4*a* and S at 4*b* Wyckoff positions having fractional coordinates (0, 0, 0) and (0, 1/2, 0), respectively. The Ni cations are partially substituted in place of strontium after constructing a 2×2×2 supercells (see Fig 1 (d, f, h)). The Ni doped SrS structure reveals that resultant alloys retain the cubic crystal structure with *Fm-3m* space group.

Table 1. Structural parameters of pure SrS and $Sr_{1-x}Ni_xS$ alloys.

Structural Parameters	SrS (Fm-3m)	Concentration of Ni atoms		
		$Sr_{0.9375}Ni_{0.0625}S$ (Fm-3m)	$Sr_{0.875}Ni_{0.125}S$ (Fm-3m)	$Sr_{0.75}Ni_{0.25}S$ (Fm-3m)
a_o (Bohr)	11.2872	10.1038	10.6934	10.9320
V_o (a.u)^3	359.5044	5620.6415	2737.5216	1306.4734
E_o (Ryd.)	-7156.779019	-111136.015933	-53909.368845	-25296.053988
B_o (GPa)	56.5488	54.5523	54.2006	58.2963
B_o'	7.3681	4.7843	5.6216	4.7607
ΔH_f (eV)	…	-1.61	-1.72	-1.79

Self-consistent-field (SCF) computations is utilized to calculate the total energy of each supercell [50, 51]. To analyze the energy versus volume curves of the Ni substituted supercells, the structures of $Sr_{1-x}Ni_xS$ were optimized in both the ferromagnetic (FM) and non-magnetic (NM) phases. The FM phase exhibited greater stability for the Ni-SrS systems, with energy values lower than (see Fig. 1 (c, e, g)) those of the NM phase. Computed optimized volumes (V_o) and energies (E_o) values are listed in Table 1. Ground state structural parameters that include lattice constant (a_o), bulk modulus (B_o) and its first order derivative, termed as pressure derivative (B_o'), is computed by fitting the total energy as function of volume in Murnaghan equation of state (EOS) (see Table 1) [52, 53].

$$E(V) = E\,(V_o) + \frac{9}{16}B_oV_o\left[\left\{\left(\frac{V_o}{V}\right)^{2/3} - 1\right\}^2 B' + \left\{\left(\frac{V_o}{V}\right)^{2/3} - 1\right\}^2 \left\{6 - 4\left(\frac{V_o}{V}\right)^{2/3}\right\}\right] \quad (2)$$

The optimized lattice constant (a_0) increases slightly with rising dopant concentration [30]. This a_0 expansion is driven by the larger atomic radii of the Ni atoms compared to the atoms they replace [54, 55]. It significantly influences the bulk modulus, providing increased resistance to compression against applied pressure, which could be desirable property for any materials consideration for practical applications [56] [57, 58].

Furthermore, formation enthalpy (ΔH_f) is computed to analyze the thermodynamic stability of studied alloys. A chemically stable material has negative ΔH_f value [59, 60]. It is calculated through following relation:

$$\Delta H_f = E_{tot}(Sr_{1-x}Ni_xS) - aE_{Ni} - bE_{Sr} - cE_S \quad (3)$$

E_{tot} expresses the total formation energy of alloys. E_{Ni}, E_{Sr} and E_S display energies of individual atoms. Number of atoms per unit cell of corresponding atom is represented through a, b and c [61]. The results clarify negative ΔH_f values, revealing thermodynamically stable alloys. It further clarifies that the reaction is exothermic during the synthesis of the materials, meaning that heat is released as the reaction proceeds. This release of heat can have significant implications on reaction kinetics, crystallization, and overall process control during synthesis [62, 63].

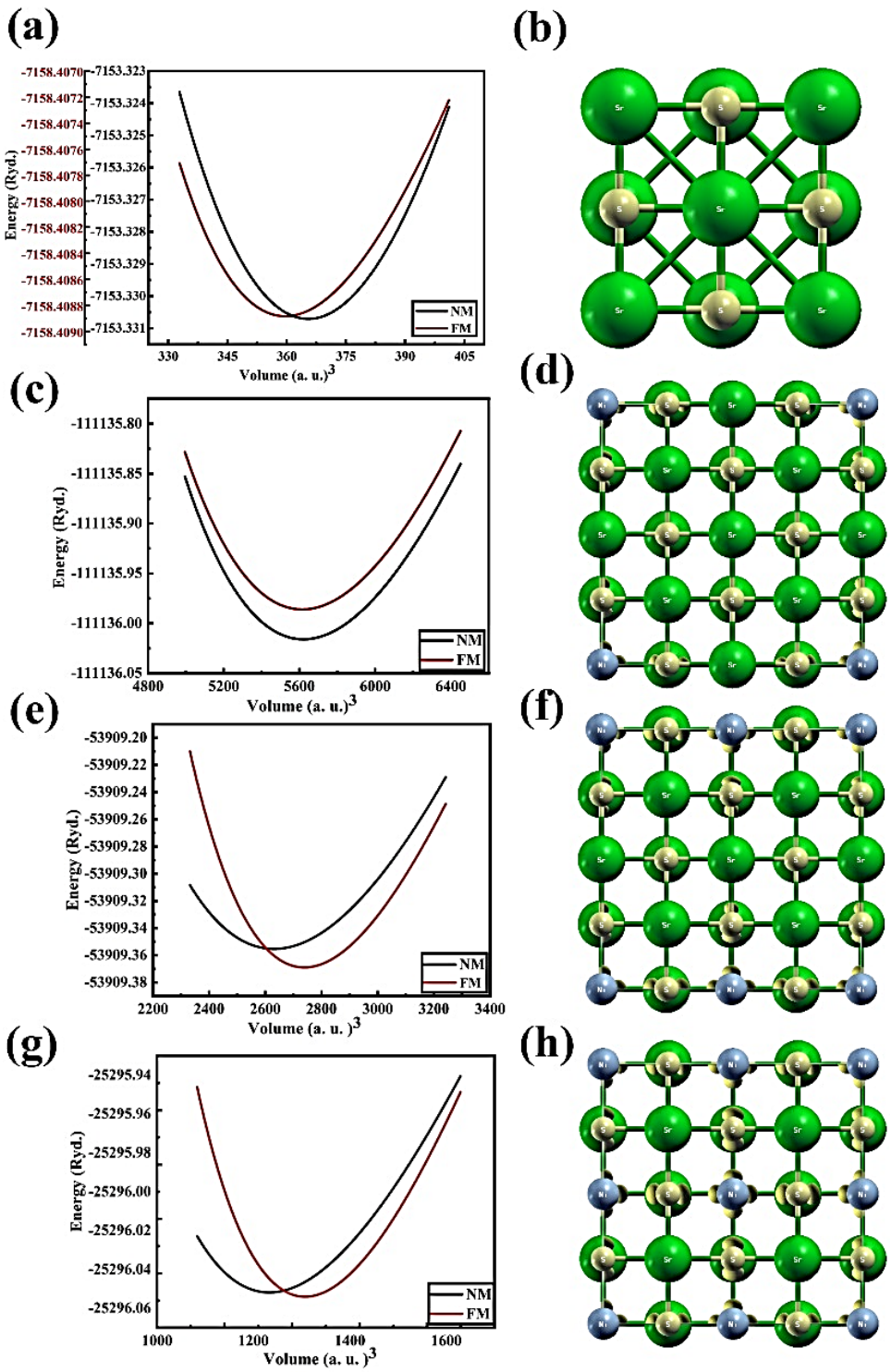

Fig. 1. The optimization and crystal lattices of (a&b) pure SrS (c&d) $Sr_{0.9375}Ni_{0.0625}S$, (e&f) $Sr_{0.875}Ni_{0.125}S$, & (g&h) $Sr_{0.75}Ni_{0.25}S$.

3.2. Electronic properties

Evaluating an alloy's electronic properties is crucial for understanding its conductivity, magnetism, reactivity, and reflectivity, enabling the design of materials tailored for specific applications [64]. For $Sr_{1-x}Ni_xS$ (x= 0%, 6.25%, 12.5% and 25%), the spin-dependent energy band structure (BS) and density of states (DOS) [65] are examined by using the well-known TB-mBJ potential. We report that pure SrS has an indirect E_g of 3.53 eV, as shown in Fig. 2(a-d), which is comparable to previously calculated value claimed in Ref. [66]. For pristine SrS, the total DOS plot is in good agreement with band structure and confirms the NM semiconducting nature. Moreover, projected (P) DOS plots highlight the major contribution of Sr-3d and S-p orbitals in forming the vicinity of F_E. This means we can introduce d states of any other suitable (Ni in this case) to tune the states in the vicinity of F_E. As predicted, the electronic properties are significantly altered through the introduction of Ni atoms into the SrS lattice and changed into dilute magnetic semiconductor (which is discussed in detail below). In result of doping, we report significant decrease in E_g values. Both spin states (up/dn) reveal semiconductive nature with direct E_g value of 1.92, 2.38 and 1.52 eV in up spin direction while 1.12, 0.95 and 0.78 eV in down spin direction for for $Sr_{0.9375}Ni_{0.0625}S$, $Sr_{0.8750}Ni_{0.1250}S$, and $Sr_{0.750}Ni_{0.250}S$, respectively as shown in Fig. 3(a-i).

The analysis of the total (T) DOS provides additional insight into the results obtained from the BS analysis. The asymmetrical plots of TDOS and confirmed the spin polarization of ternary alloys [66]. We report a strong contribution of Ni to the electronic states near the F_E that further implies the observed reduction in E_g. The PDOS provides a more detailed insight about contribution of individual atomic orbitals [67], which further clarifies the hybridization phenomenon. For all studied ternary alloys, PDOS analysis reveals that the VB primarily composed of Ni-3d and S-3p/3d states in both spins as shown in Fig. 4(a-i). No significant contribution of Sr-5s states is observed. Ni-3d orbitals strongly hybridize with the S-3p and S-3d states near F_E in VB, playing a significant role in spin splitting for all studied alloys. On the other hand, 3d orbitals of Ni also contribute prominently in CB minima of spin down channel.

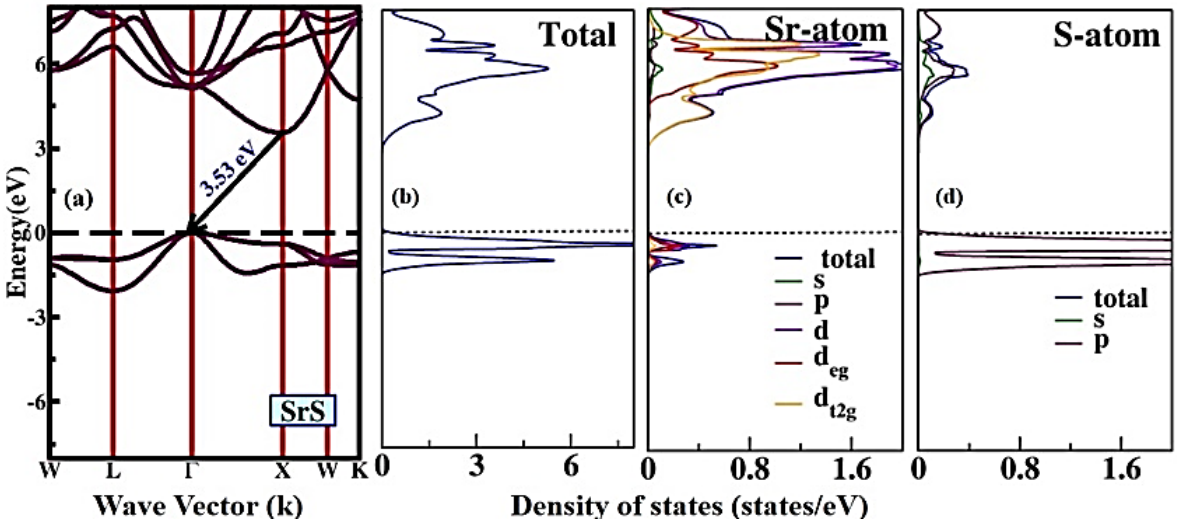

Fig. 2. (a) BS of pure SrS and (b-d) TDOS of pure SrS.

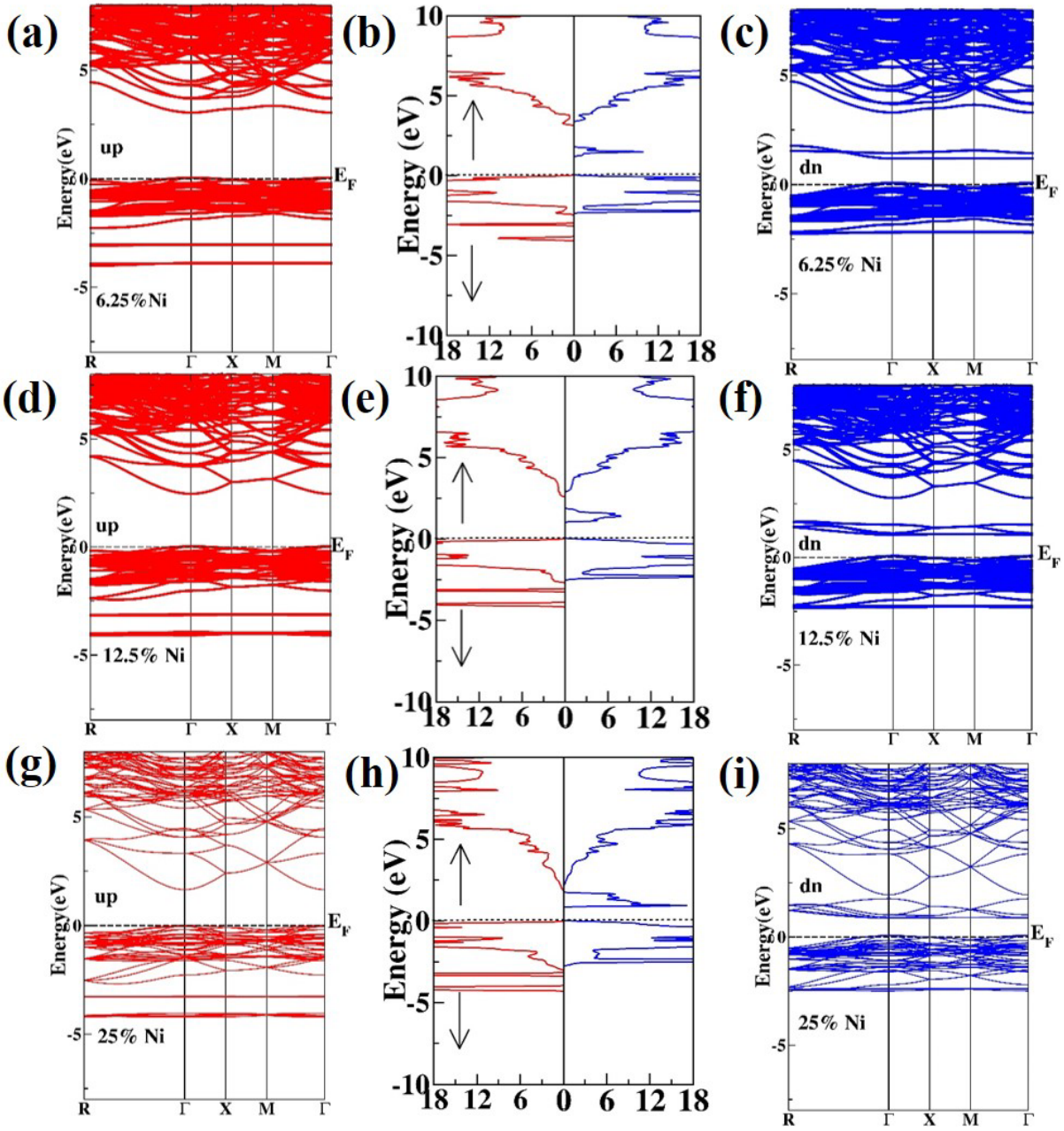

Fig. 3. Spin-resolved BS (left and right section) and TDOS plots (central section) of (a) $Sr_{0.9375}Ni_{0.0625}S$ (b) $Sr_{0.8750}Ni_{0.1250}S$ (c) $Sr_{0.750}Ni_{0.250}S$.

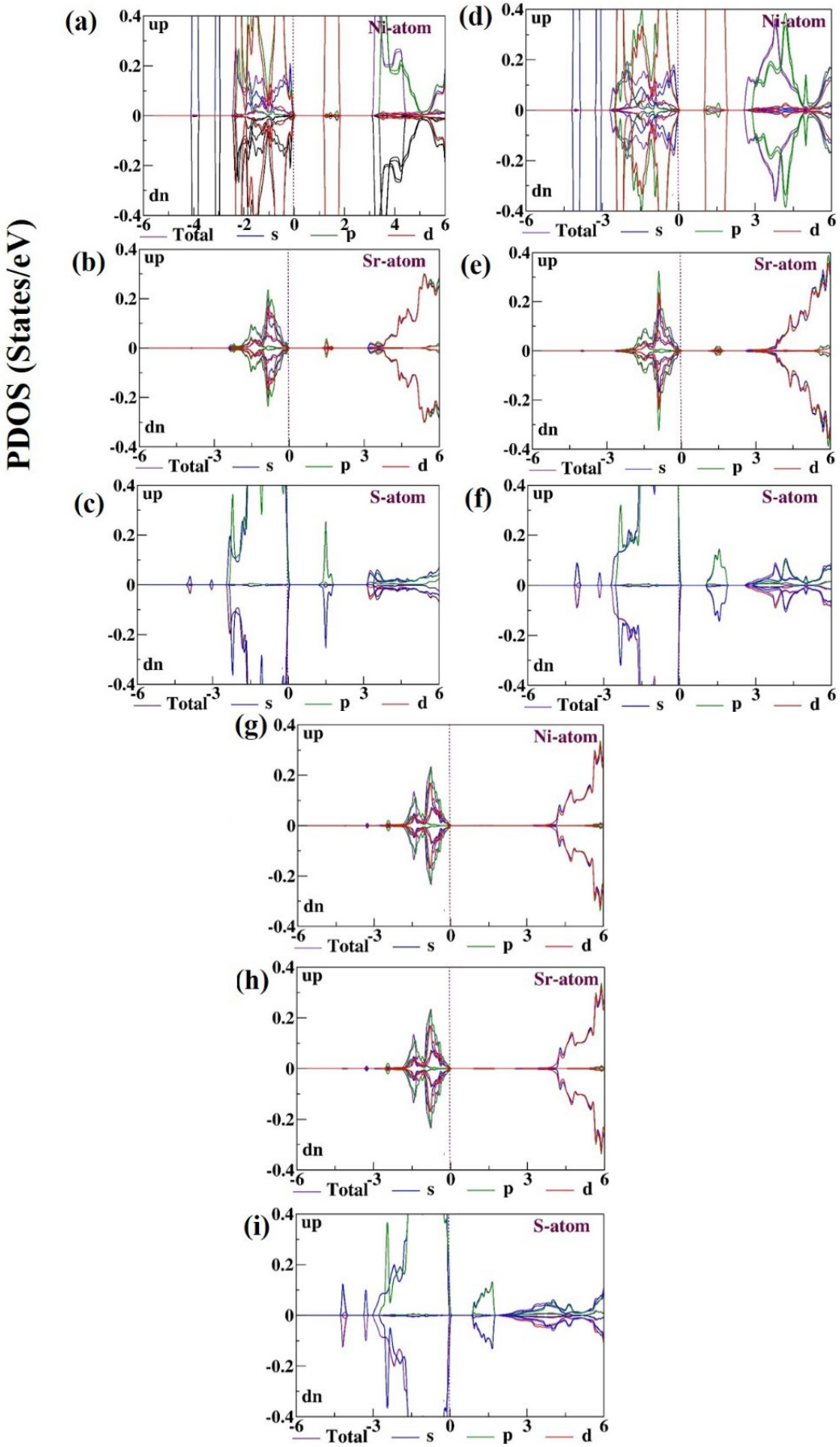

Fig. 4. Spin-resolved projected DOS of (a-c) $Sr_{0.9375}Ni_{0.0625}S$ (d-f) $Sr_{0.8750}Ni_{0.1250}S$ (g-i) $Sr_{0.750}Ni_{0.250}S$.

3.3. Magnetic properties

DOS analysis confirms that Ni-doped SrS systems display magnetic behavior, necessitating the need to investigate the origin and doping-dependent magnetic properties. The total magnetic moments (μ_B) of the Ni-doped SrS systems, as well as the local μ_B of the Ni dopants, Sr atoms, and neighboring S atoms are tabulated in Table 2. Mostly, the magnitude of the total μ_B corresponds to the number of unpaired electrons or holes introduced in these systems. The introduction of Ni atoms at Sr sites, contribute the unpaired d-electrons to the system, resulting in integral values of total μ_B. It confirms the Slater-Pauling criteria that interprets the total μ_B value of semiconductor in integers [68]. When comparing the local μ_B in each doped system, it becomes evident that the Ni dopants contribute large portion to the overall μ_B, playing a key role in the magnetic interactions, which is ensured from spin magnetic densities ((see Fig 1 (b, d, f))). Furthermore, a minor contribution in μ_B arises from other Sr atoms and adjacent S atoms, suggesting that the magnetic behavior is governed by a hole-mediated p-d exchange coupling mechanism. For 6.25% and 12.5% doping content, positive μ_B values exist for individual atoms, this indicates that Sr and S atoms are ferromagnetically coupled with the Ni dopants, where positive values exist [68]. However, at 25% doping, Sr (with negative moment values) revealed ferrimagnetic/antiferromagnetic coupling with the other atoms in the system [69]. In summary, the Ni-doped SrS material demonstrates promise for spintronic applications, owing to its significant net spin magnetic moment.

Table 2. Computed magnetic moments for $Sr_{1-x}Ni_xS$ (x= 6.25%, 12.5% and 25%).

Compounds	Interstitial	Ni	Sr	S	Total
$Ni_{0.0625}Sr_{0.9375}S$	0.10589	1.39685	0.00045	0.08300	2.00742
$Ni_{0.125}Sr_{0.875}S$	0.23109	1.38905	0.00759	0.00032	3.96147
$Ni_{0.25}Sr_{0.75}S$	0.41613	1.36377	-0.00065	0.14246	7.59088

3.4. Optical properties

Exploring the optical response of alloys interprets the information about how a material behaves when it exposed to light energy $(E = hf)$ of different wavelengths [70][71, 72][73]. Particularly, after analyzing the significant drop in E_g up to the range of visible – infrared range, it became pertinent for us to explore their optical response.

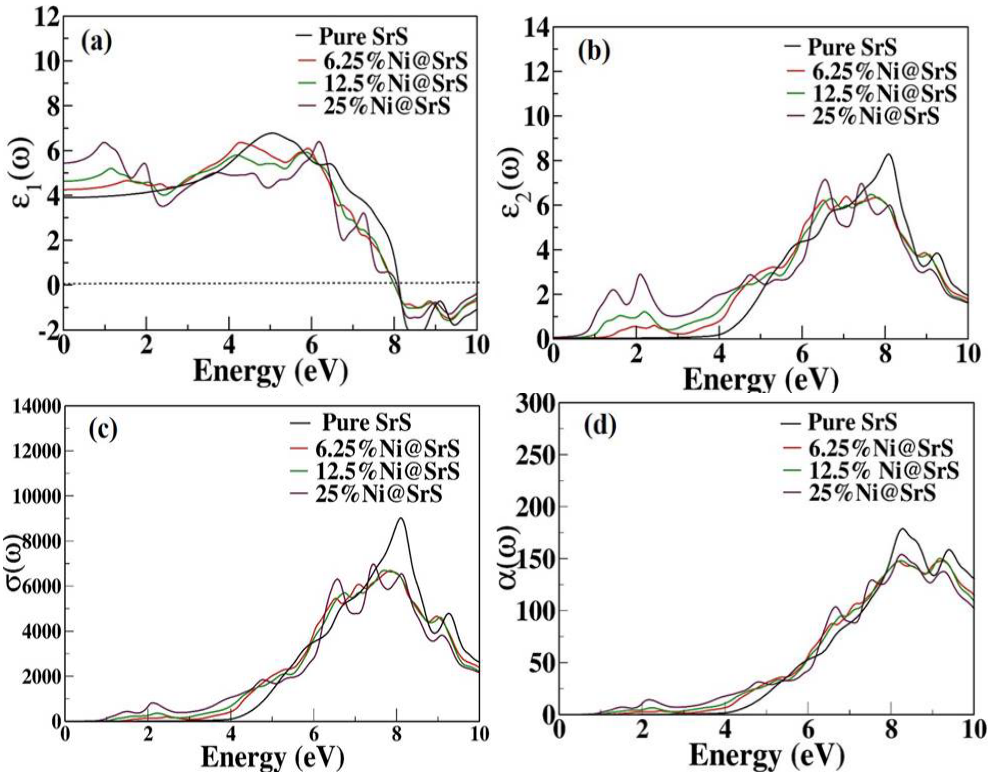

Fig. 5. Optical characteristics of pure and $Sr_{1-x}Ni_xS$ (a) ε_1 (ω), (b) ε_2 (ω), (c) σ (ω) and (d) α (ω).

A complex symmetric second-order tensor is utilized to characterize the optical properties that is represented by dielectric function ε(ω). It elaborates the linear response to the incoming electromagnetic radiations.

The direct interaction of the electronic system to an external electric field is explained by this tensor. The ε(ω) of alloys can be determined as [74]:

$$\varepsilon(\omega) = \varepsilon_1(\omega) + i\varepsilon_2(\omega) \tag{4}$$

The Kramers-Kronig (KK) expression is applied to compute the real component ($\varepsilon_1(\omega)$) of complex dielectric constant. $\varepsilon_1(\omega)$ is the integral transformation of the imaginary component ($\varepsilon_2(\omega)$) [75]. Mathematically can be represented as [76-78]:

$$\varepsilon_1(\omega) = 1 + \frac{2}{\pi} p \int_0^{\Theta} \frac{\omega'(\varepsilon_2(\omega'))}{\omega'^2 - \omega^2} d\omega' \tag{5}$$

$$\varepsilon_2(\omega) = \frac{e^2\hbar}{\pi m^2 \omega^2} \sum_{vc} \int |n, n'(k,q)|^2 \, [\omega n, n'(k) - \omega] \, d^3k \tag{6}$$

The subsequent equations were used to compute optical features based on the dielectric constants ($\varepsilon_1(\omega)$ and $\varepsilon_2(\omega)$) [79, 80].

$$\sigma(\omega) = \frac{2W_{cv}\hbar\omega}{\vec{E}^2} \tag{7}$$

$$n(\omega) = \left[\frac{\sqrt{\{\varepsilon_1^2(\omega)+\varepsilon_2^2(\omega)\}}+\varepsilon_1(\omega)}{2}\right]^{1/2} \tag{8}$$

$$R = \frac{(n-1)^2+k^2}{(n+1)^2+k^2} = \left|\frac{n'-1}{n'+1}\right| \tag{9}$$

$$\alpha(\omega) = \frac{4\pi k}{\lambda} \tag{10}$$

$$k(\omega) = \left[\frac{\{\varepsilon_1^2(\omega)+\varepsilon_2^2(\omega)\}^{\frac{1}{2}}-\varepsilon_1(\omega)}{2}\right]^{1/2} \tag{11}$$

$\varepsilon_1(\omega)$ elucidates the polarization of a material that occurs in response of applied electric field, which results in the formation of electric dipoles within the material. We theoretically predict the $\varepsilon_1(0)$ value for pure SrS to be 3.93, comparable to previously reported value [81]. For $Sr_{0.9375}Ni_{0.0625}S$, $Sr_{0.875}Ni_{0.125}S$, and $Sr_{0.75}Ni_{0.25}S$, the $\varepsilon_1(0)$ values are 4.4, 4.76, and 5.53, respectively (see Table 3). As the photon energy increases, values of $\varepsilon_1(\omega)$ diminishes. Beyond 7.95 eV point, the values turn negative for all doped alloys, indicating the metallic behavior in this range (see Fig. 5a). Pure SrS exhibited metallic behavior at 8.1 eV. Values of $\varepsilon_1(\omega)$ below the zero (negative) arise from the interplay between large effective masses with electrons and the applied electric field [82]. The absorptive behavior of a material and its relationship to the BS is illustrated through the $\varepsilon_2(\omega)$ (see Fig. 5b). The threshold $\varepsilon_2(\omega)$ values drop with the increase in Ni dopant's concentration, which is consistent with electronic properties. For pure, 6.25%, 12.5%, and 25% doping levels, maximum $\varepsilon_2(\omega)$ is observed at energy points of 8.26, 8.15, 8.2, and 8.25 eV, respectively. The strongest $\varepsilon_2(\omega)$ peaks in the $Sr_{1-x}Ni_xS$ (x = 6.25%, 12.5%, 25%) spectra are located within 7.2–9.46 eV. A decreasing trend in peak intensity after adding dopants is because of the alternations in the electronic structure, leading to reduce the interactions with the incoming electromagnetic field [30].

A material is facilitated by free optically active electrons that are produced when photons are captivated by outer electrons and force them to shift to the CB, the phenomenon called optical conductivity σ(ω). The peak patterns of σ(ω) are analogous to those in the graphs of α(ω) and $\varepsilon_2(\omega)$. σ(ω) is associated with $\varepsilon_2(\omega)$ as [83]:

$$\sigma(\omega) = \frac{\omega\varepsilon_2(\omega)}{4\pi} \tag{12}$$

For pure SrS, $Sr_{0.9375}Ni_{0.0625}S$, $Sr_{0.875}Ni_{0.125}S$, and $Sr_{0.75}Ni_{0.25}S$, σ(ω) begins at 4.2, 2.1, 2.16 and 1.36 eV and rapidly rises, reaching to peak values of 9066.42, 6900, 6800 and 7066 (1/Ω.cm) at energy levels of 8.08, 7.85, 7.71, and 7.41 eV correspondingly, exposing maximum conductivity in UV span (see Fig. 5c). The α(ω) measures the capability of a material to captivate light over a specific thickness, with higher α(ω) values indicating greater light absorption per unit thickness. A decreasing trend is observed in the α(ω) from 161.42 $\times 10^4$ to 138.92$\times 10^4$ cm^{-1} within 9-9.61 eV as the Ni concentration is elevated from 0 to 25 %, after which the curves declined (see Fig. 5d). These energy values lie within the UV spectrum. The minimal light scattering at these values suggests the potential for optoelectronic usages. As α(ω) and $\varepsilon_2(\omega)$ both relies on interband excitations and de-excitations, hence a similar pattern is noted (see Fig. 5(b, d)). The incorporation of Ni dopants leads to a red shift in absorption characteristics. This change is caused by the modification of energy due to the dopants, which is created by the optical transitions. The absorption values reveal that the materials may be beneficial in applications like of solar cell, optical filters, UV LASERs and other optical sensors. The k(ω), illustrates the absorption capacity of a substance. It is related to absorption coefficient as [84]:

$$k\ (\omega) = \frac{\lambda\, \alpha\ (\omega)}{4\pi} \tag{13}$$

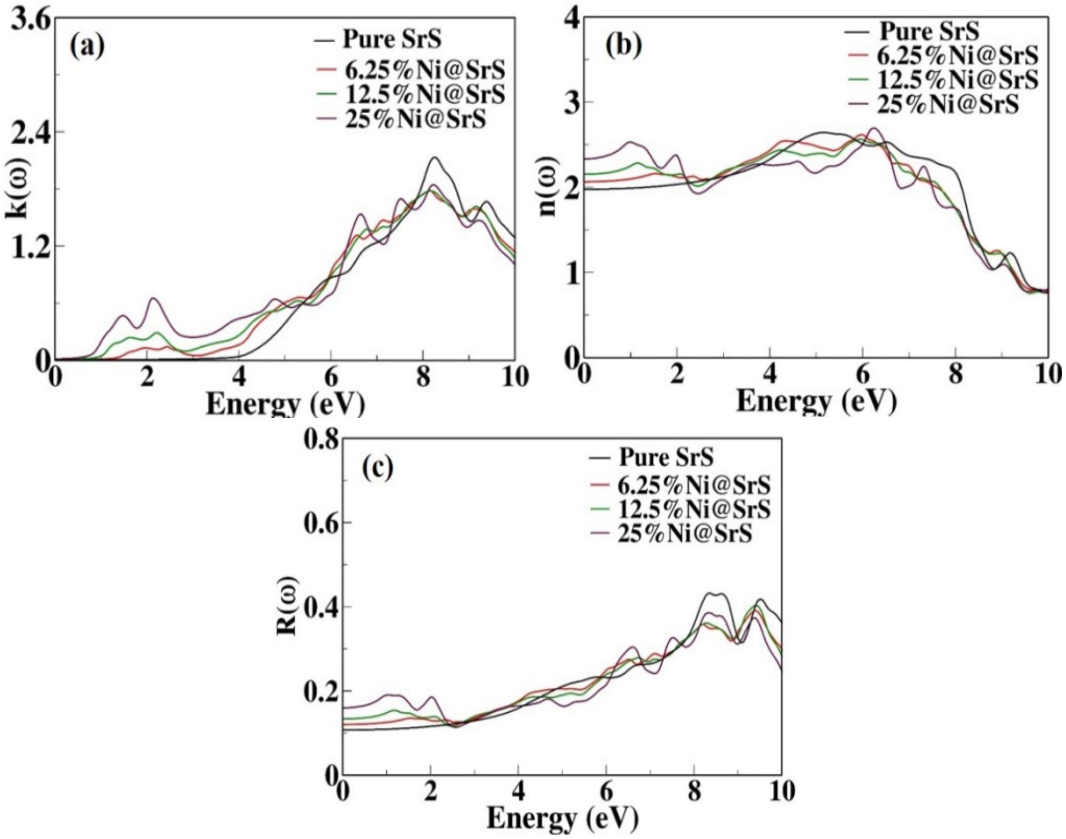

Fig. 6. Optical characteristics of pure and $Sr_{1-x}Ni_xS$ (a) k (ω), (b) n (ω), and (c) R (ω).

In the k(ω) spectrum (see Fig. 6a), onset edges are found to be on same energies relevant to E_g values, while highest values are found to be 2.16, 1.80, and 1.82 and 1.88 at 8.21, 8.0 ,8.2 and 8.23 eV for pure SrS, $Sr_{0.9375}Ni_{0.0625}S$, $Sr_{0.875}Ni_{0.125}S$, and $Sr_{0.75}Ni_{0.25}S$, respectively. Hence this trend of k(ω) plot is similar to that of $\varepsilon_2(\omega)$ plot. The n(ω) explains how a photon moves inside a material and is influenced by its optical properties, density, and composition. Transparent materials typically have very low n(ω) values (~1.0), while highly absorbent materials exhibit higher n(ω) values. The static refractive index n(0) values for pure SrS, 6.25%, 12.5%, and 25% Ni doped SrS are 2.00, 2.10,

2.18 and 2.35, correspondingly (see Table 3). High values are observed in middle UV energy region and after that decreasing trend is observed with fluctuating peaks (see Fig. 6b) in far UV range. When light interacts with materials, its energy is divided among absorption, reflection, and transmission. Fig. 6c illustrates the reflection R(ω) of light as it interacts with the surface of material [85]. The static reflection R(0) value are 0.11, 0.12, 0.14 and 0.16 for pure, 6.25%, 12.5%, and 25% doping levels, in their respective order (see Table 3). The curves steadily increase after 2 eV with oscillating peaks up to maximum R(ω). The extreme R(ω) values observed in UV spectrum having values of 44% (at 8.3), 39% (at 9.4), 40% (at 9.35), 38% (at 8.23 eV) for pure, $Sr_{0.9375}Ni_{0.0625}S$, $Sr_{0.875}Ni_{0.125}S$, and $Sr_{0.75}Ni_{0.25}S$, respectively. In case of 25% doping concentration, it is worth noting that the maximum R(ω) is noted in the span where $\varepsilon_1(\omega) < 0$ (see Fig 5a, 6c). Our optical properties' analysis reveals similar like trend as most of the industry-oriented materials. A material with low synthetic cost with easy to achieve stable cubic configuration, coupled with low energy optical absorption threshold can make a strong case for Ni doping as effective way to obtain practical materials.

Table 3. The static values of $\varepsilon_1(0)$, n(0), and R(0) of pure SrS and $Sr_{1-x}Ni_xS$ alloys.

Alloys	$\varepsilon_1(0)$	n(0)	R(0)
Pure SrS	3.93	2.00	**0.11**
$Sr_{0.94}Ni_{0.06}S$	4.4	2.10	0.12
$Sr_{0.87}Ni_{0.12}S$	4.76	2.18	0.14
$Sr_{0.75}Ni_{0.25}S$	5.53	2.35	0.16

3.5. Thermoelectric properties

The ever-rising demand for energy and the need to minimize heat waste in electronic systems have driven research into the thermoelectric properties of compounds. TE substances can change waste heat into energy [86]. As we mentioned earlier, Ni-doped SrS exhibits a reduction in the band gap; therefore, doped systems are expected to depict improved thermoelectric behavior for designing efficient TE devices. For pure and doped alloys, TE features are plotted against temperature range (200-800 K) as shown in Fig. 7 & Fig.8. Semi-classic BoltzTraP code has been used for their TE evaluation [45]. Electrical conductivity is a useful parameter to illustrate effect of electrons moments in probed alloys. The significantly higher values of σ are basic requirement of proficient thermoelectric devices. According to Joule's effect, high values of electric conductivity reduce the heat wastage during the operation of conductors. Pure SrS has lower value of electric conductivity as compared to doped alloys. The value of electrical conductivity exhibits an increasing trend with increasing Ni dopant content in SrS. This might be due to reason that doping element introduces more free charge carriers in crystal lattice which are essential for electrical conductivity. The peak values of σ are recorded as: 0.68, 0.92, 0.95 and 1.02 ($10^{19}.\Omega^{-1}.cm^{-1}.s^{-1}$) for pure, $Sr_{0.9375}Ni_{0.0625}S$, $Sr_{0.875}Ni_{0.125}S$ and $Sr_{0.75}Ni_{0.25}S$ alloys at 800 K as shown in Fig.7(a). The efficiency of a thermoelectric device requires low thermal conductivity (κ_e) to maintain a temperature gradient.

The κ_e exhibits similar increasing trend as the electrical conductivity as shown in Fig. 7(b). Pure SrS has higher value of κ_e as compared to doped alloys. The substitution of Ni helps in lowering the thermal conductivity value that is desirable for efficient TE materials. The maximum values of κ_e are computed as: 4.88, 4.00, 3.86 and 4.48 ($10^{14}.W/m.K^2.s$) for pure, $Sr_{0.9375}Ni_{0.0625}S$, $Sr_{0.875}Ni_{0.125}S$ and $Sr_{0.75}Ni_{0.25}S$ alloys, respectively at 800 K. The Seebeck coefficient or thermopower (S) is a key parameter in deciding the efficacy of a material for its applicability in thermoelectric devices [34]. Materials exhibiting larger values of Seebeck coefficient are expected to have high Figure of merit (ZT) and ultimately greater ability for the transition of thermal energy into electric energy. The Seebeck coefficient for pure SrS has nearly linear trend with temperature. While in case of doped alloys the Seebeck coefficient exhibits a tremendous growth with temperature and Ni content. The obtained values of S are: 259.0, 188.792, 185.019 and 203.753 (μV/K) for pure, $Sr_{0.9375}Ni_{0.0625}S$, $Sr_{0.875}Ni_{0.125}S$ and $Sr_{0.75}Ni_{0.25}S$ alloys (see Fig. 7(c)), correspondingly, at 800 K. The positive values

of S within entire temperature indicates that all studied compositions have p-type semiconductive nature [82].

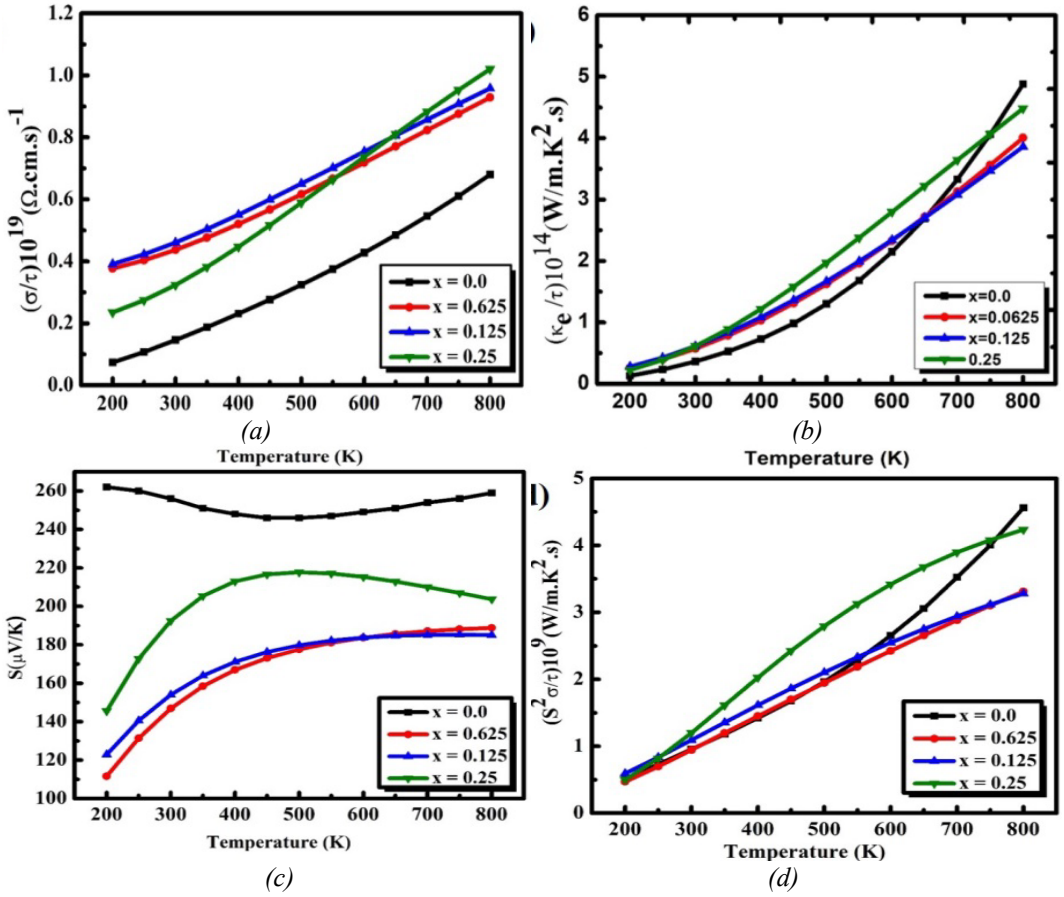

Fig. 7. Thermoelectric characteristics of pure and $Sr_{1-x}Ni_xS$ (a) σ/τ (b) κ_e/τ (c) S (d) PF.

The power factor ($S^2\sigma/\tau$) is a keynote parameter for measuring transport characteristics of studied alloys. It is noted that PF rapidly elevates with temperature (see Fig. 7(d)). Among doped alloys, $Sr_{0.75}Ni_{0.25}S$ has highest value of PF. We have shown that the higher Ni content is optimal in improving the electrical conductivity and $S^2\sigma/\tau$. The obtained values of PF are: 4.56, 3.31, 3.27 and 4.23×10^{11}(W /k^2.cm.s) for pure, $Sr_{0.9375}Ni_{0.0625}S$, $Sr_{0.875}Ni_{0.125}S$ and $Sr_{0.75}Ni_{0.25}S$ alloys, respectively at 800 K. The most important factor in thermoelectric power generation (TPG), is figure of merit denoted by relation $ZT=S^2\sigma T/\kappa$. Substances exhibiting larger ZT values are regarded as efficient TE materials [86]. The peak values of ZT are recorded as: 0.74, 0.66, 0.67 and 0.75 for pure, $Sr_{0.9375}Ni_{0.0625}S$, $Sr_{0.875}Ni_{0.125}S$ and $Sr_{0.75}Ni_{0.25}S$ alloys, respectively at 800 K as shown in Fig. 8. Highest value of ZT is obtained for highest Ni content that highlights the impact of Ni substitution in improving the TE profile of pure SrS. The values of TE terms at various temperatures are summarized in Table 4. This implies that our selected approach in this research is successful in fine tuning the transport properties of Ni-SrS alloys, which will surely attract experimental scientists to explore their viability for practical applications.

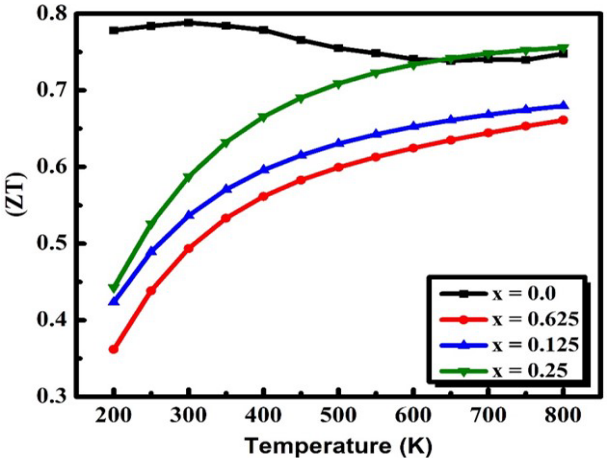

Fig. 8. ZT of pure and $Sr_{1-x}Ni_xS$.

Table 4. Computed TE parameters

Thermoelectric parameters	S μV/K		$(\sigma/\tau) \times 10^{19}$ $(\Omega\ cm\ s)^{-1}$		PF $(S^2\sigma/\tau) \times 10^{11}$(W /$k^2$.cm.s)		ZT $(S^2\sigma T/\kappa_e)$		$(\kappa_e/\tau)\times 10^{14}$(W/$k^2$.m. s)	
Temperature (K)	300	800	300	800	300	800	300	800	300	800
SrS	256	259	0.145	0.68	0.95	4.56	0.78	0.74	0.36	4.88
$Sr_{0.94}Ni_{0.06}S$	146.88	188.79	0.43	0.928	0.94	3.31	0.49	0.66	0.57	4.00
$Sr_{0.87}Ni_{0.12}S$	154.06	185.01	0.46	0.95	1.09	3.27	0.53	0.68	0.61	3.86
$Sr_{0.75}Ni_{0.25}S$	192.50	203.75	0.32	1.02	1.19	4.23	0.58	0.75	0.61	4.48

4. Conclusion

This study employs DFT to investigate the physical properties of pure and nickel-substituted strontium sulfide at various concentrations. The $Sr_{1-x}Ni_xS$ (x = 6.25%, 12.5%, 25%) alloys exhibit thermodynamic stability, as evidenced by their negative enthalpy of formation. The electronic properties of pure SrS reveal an indirect E_g of 3.53 eV, while the Ni-doped systems exhibit ferromagnetic semiconducting behavior, with a progressive decrement in the E_g as the Ni concentration elevated from 6.25% to 25%. The ferromagnetism is primarily attributed to the Ni 3d states, as confirmed by spin-magnetic analysis. Optical properties indicate that the alloys are active across the UV to visible spectrum. Additionally, the high ZT (~0.75) highlights the potential of these alloys for thermoelectric power generation applications. Overall, the results demonstrate that the investigated alloys are promising for spintronic, optoelectronic, and thermoelectric device applications.

Acknowledgements

This research project was funded by the Deanship of Scientific Research and Libraries, Princess Nourah bint Abdulrahman University, through the Program of Research Project Funding After Publication, grant No (RPFAP-27-1445).

References

[1] Ohno, H., Science, 1998. **281**(5379): p. 951-956; https://doi.org/10.1126/science.281.5379.951
[2] Quesada, A., et al., European Physical Journal B: Condensed Matter, 2007. **59**(4); http://dx.doi.org/10.1140/epjb/e2007-00063-1
[3] Bezzine, K., et al., Journal of Magnetism and Magnetic Materials, 2022. **563**: p. 169910; https://doi.org/10.1016/j.jmmm.2022.169910
[4] Awschalom, D.D., M.E. Flatté, Nature Physics, 2007. **3**(3): p. 153-159; http://dx.doi.org/10.1038/nphys551
[5] Jan, H.U., et al., Solid State Communications, 2024. **391**: p. 115627; https://doi.org/10.1016/j.ssc.2024.115627
[6] Mahmood, Q., Hassan, M. (2017), Journal of Alloys and Compounds, 704, 659-675; https://doi.org/10.1016/j.jallcom.2017.02.097
[7] Bourouis, C., A. Meddour, Journal of magnetism and magnetic materials, 2012. **324**(6), p.1040-1045; https://doi.org/10.1016/j.jmmm.2011.10.022
[8] Ivanov, V. A., Ugolkova, E. A., Pashkova, O. N., Sanygin, V. P., Padalko, A. G. (2006), Journal of Magnetism and Magnetic Materials, 300(1), e32-e36; https://doi.org/10.1016/j.jmmm.2005.11.034
[9] Sato, K., Bergqvist, L., Kudrnovský, J., Dederichs, P. H., Eriksson, O., Turek, I., Zeller, R. (2010), Reviews of Modern Physics, 82(2), 1633-1690; https://doi.org/10.1103/RevModPhys.82.1633
[10] Haq, B. U., Ahmed, R., Shaari, A., Ali, N., Al-Douri, Y., Reshak, A. H. (2016), Materials Science in Semiconductor Processing, 43, 123-128; https://doi.org/10.1016/j.mssp.2015.12.010
[11] Tanveer, W., Faridi, M. A., Noor, N. A., Mahmood, A., Amin, B. (2015), Current Applied Physics, 15(11), 1324-1331; https://doi.org/10.1016/j.cap.2015.07.016
[12] Hamidane, N., Baaziz, H., Ocak, H. Y., Baddari, K., Uğur, Ş., Uğur, G., Charifi, Z. (2020), Journal of Superconductivity and Novel Magnetism, 33, 3263-3272; https://doi.org/10.1007/s10948-020-05527-w
[13] Mahmood, Q., Khalil, S., Hassan, M., Laref, A. (2018), Materials Research Bulletin, 107, 225-235; https://doi.org/10.1016/j.materresbull.2018.07.039
[14] Doumi, B., Tadjer, A., Dahmane, F., Mesri, D., Aourag, H. (2013), Journal of superconductivity and novel magnetism, 26, 515-525.15; https://doi.org/10.1007/s10948-012-1808-6
[15] Alsaad, A. (2009), Physics Research International, 2009(1), 406095; https://doi.org/10.1155/2009/406095
[16] Hamidane, O., Meddour, A., Gous, M. H., Bourouis, C. (2021), Journal of Superconductivity and Novel Magnetism, 34, 179-192; https://doi.org/10.1007/s10948-020-05706-9
[17] Nazir, S., Ikram, N., Tanveer, M., Shaukat, A., Saeed, Y., Reshak, A. H. (2009), The Journal of Physical Chemistry A, 113(20), 6022-6027; https://doi.org/10.1021/jp900698q
[18] Boutaleb, M., Doumi, B., Sayede, A., Tadjer, A., Mokaddem, A. (2015), Journal of Superconductivity and Novel Magnetism, 28, 143-150; https://doi.org/10.1007/s10948-014-2825-4
[19] Shahjahan, M., Razzakul, I. M., Rahman, M. M. (2016), Computational Condensed Matter, 9, 67-71; https://doi.org/10.1016/j.cocom.2016.10.001
[20] Bordjiba, Z., Meddour, A., Bourouis, C. (2018), Journal of Superconductivity and Novel Magnetism, 31, 2261-2270; https://doi.org/10.1007/s10948-017-4495-5
[21] Zoubir, M. H., Cheref, O., Merabet, M., Benalia, S. E., Djoudi, L., Rached, D., Boucharef, M. (2024), Revista Mexicana de Física, 70(2 Mar-Apr), 020501-1; https://doi.org/10.31349/RevMexFis.70.020501
[22] Gueddim, A., Madjet, M. E., Zerroug, S., Bouarissa, N. (2016), Optical and Quantum Electronics, 48, 1-13; https://doi.org/10.1007/s11082-016-0818-1
[23] Ullah, H., Inayat, K., Khan, S. A., Mohammad, S., Ali, A., Alahmed, Z. A., Reshak, A. H. (2015), Journal of Magnetism and Magnetic Materials, 385, 27-31; https://doi.org/10.1016/j.jmmm.2015.02.069

[24] Tanji, K., et al., Reaction Kinetics, Mechanisms and Catalysis, 2023. **136**(2): p. 1125-1142; https://doi.org/10.1007/s11144-023-02385-0
[25] Geisz, J., D. Friedman, Semiconductor Science and Technology, 2002. **17**(8): p. 769; http://dx.doi.org/10.1088/0268-1242/17/8/305
[26] Taoufiq, M., et al., Optical Materials, 2024. **147**: p. 114607; https://doi.org/10.1016/j.optmat.2023.114607
[27] Slipukhina, I., D. Bercha, Physica Status Solidi (B), 2007. **244**(2): p. 650-668; https://doi.org/10.1002/pssb.200642263
[28] Cowley, R., Philosophical Magazine, 1965. **11**(112): p. 673-706; https://doi.org/10.1080/14786436508230077
[29] Murase, K., Ferroelectrics, 1981. **35**(1): p. 67-72; https://doi.org/10.1080/00150198108017666
[30] Serradj, F., et al., Physica B: Condensed Matter, 2024. **689**: p. 416204; https://doi.org/10.1016/j.physb.2024.416204
[31] Elaggoune, W., F. Ersan, A. Meddour, RSC Advances, 2024. **14**(29): p. 20668-20682; https://doi.org/10.1039/d4ra04352a
[32] Labidi, S., et al., Computational Materials Science, 2011. **50**(3): p. 1077-1082; https://doi.org/10.1016/j.commatsci.2010.11.004
[33] Gao, G., et al., Physical Review B—Condensed Matter and Materials Physics, 2007. **75**(17): p. 174442; https://doi.org/10.1103/PhysRevB.75.174442
[34] Yari, A., A. Boochani, S. Rezaee, Chemical Physics, 2021. **551**: p. 111355; https://doi.org/10.1016/j.chemphys.2021.111355
[35] Bhattacharjee, R., S. Chattopadhyaya, Materials Chemistry and Physics, 2017. **199**: p. 295-312; https://doi.org/10.1016/j.matchemphys.2017.06.057
[36] Nikšić, T., D. Vretenar, P. Ring, Progress in Particle and Nuclear Physics, 2011. **66**(3): p. 519-548; https://doi.org/10.1016/j.ppnp.2011.01.055
[37] Fernando, G.W., Chapter 6 - Generalized Kohn–Sham Density Functional Theory via Effective Action Formalism, in Handbook of Metal Physics, G.W. Fernando, Editor. 2008, Elsevier. p. 131-156; https://doi.org/10.1016/S1570-002X(07)00006-7
[38] Butera, V., Physical Chemistry Chemical Physics, 2024; https://doi.org/10.1039/D4CP00266K
[39] Blaha, P., et al., The Journal of Chemical Physics, 2020. **152**(7); https://doi.org/10.1063/1.5143061
[40] Schwarz, K., P. Blaha, G.K. Madsen, Computer Physics Communications, 2002. **147**(1-2): p. 71-76; https://doi.org/10.1016/S0010-4655(02)00206-0
[41] E. Wimmer, Krakauer, H. Weinert, M. Freeman, A. J., Phys. Rev. B, 1982. 24: p. 864—875; https://link.aps.org/doi/10.1103/PhysRevB.24.864
[42] Schwarz, K., P. Blaha, Computational Materials Science, 2003. **28**(2): p. 259-273; https://doi.org/10.1016/S0927-0256(03)00112-5
[43] Shoukat, L., et al., Journal of Ovonic Research, 2022. 18(5); https://doi.org/10.15251/JOR.2022.185.649
[44] Noor, N.A., et al., Physica B: Condensed Matter, 2012. **407**(6): p. 943-952 DOI: https://doi.org/10.1016/j.physb.2011.12.107
[45] Pizzi, G., et al., Computer Physics Communications, 2014. **185**(1): p. 422-429; https://doi.org/10.1016/j.cpc.2013.09.015
[46] Lucarini, V., et al., Kramers-Kronig relations in optical materials research. Vol. 110. 2005: Springer Science & Business Media; http://dx.doi.org/10.1007/b138913
[47] Ambrosch-Draxl, C., J.O. Sofo, Computer physics communications, 2006. **175**(1): p. 1-14; http://dx.doi.org/10.1016/j.cpc.2006.03.005
[48] Arshad, M., et al., Physica B: Condensed Matter, 2025. **696**: p. 416629; https://doi.org/10.1016/j.physb.2024.416629
[49] Chang, S., et al., Materials Advances, 2022. **3**(16): p. 6529-6538; https://doi.org/10.1039/D2MA00617K
[50] Debnath, B., et al., Physica B: Condensed Matter, 2018. **530**: p. 53-68; https://doi.org/10.1016/j.physb.2017.10.014

[51] Debbarma, M., et al., Journal of Alloys and Compounds, 2018. **748**: p. 446-463; https://doi.org/10.1016/j.jallcom.2018.03.093
[52] Shahid, S., et al., Physica B: Condensed Matter, 2024. **694**: p. 416388; https://doi.org/10.1016/j.physb.2024.416388
[53] Birch, F., Journal of Applied Physics, 1938. **9**(4): p. 279-288; https://doi.org/10.1063/1.1710417
[54] Doumi, B., et al.,. The European Physical Journal B, 2015. **88**: p. 1-9; https://doi.org/10.1140/epjb/e2015-50746-9
[55] Poonam, P., H.S. Saini, M.K. Kashyap, AIP Conference Proceedings. 2020. AIP Publishing; https://doi.org/10.1063/5.0017730
[56] Khanzadeh, M., G. Alahyarizadeh, Ceramics International, 2021. **47**(7): p. 9990-10005; https://doi.org/10.1016/j.ceramint.2020.12.145
[57] Bhojani, A.K., H.R. Soni, P.K. Jha, AIP Advances, 2020. **10**(1); https://doi.org/10.1063/1.5121832
[58] Afzal, F., et al., Physica B: Condensed Matter, 2025. **696**: p. 416631; https://doi.org/10.1016/j.physb.2024.416631
[59] Ahmed, R., et al., Journal of Materials Research and Technology, 2023. **24**: p. 4808-4832; https://doi.org/10.1016/j.jmrt.2023.04.147
[60] Gong, S., et al., JACS Au, 2022. **2**(9): p. 1964-1977; https://doi.org/10.1021/jacsau.2c00235
[61] Saleem, S., et al., Physica Scripta, 2022. **97**(9): p. 095817; http://dx.doi.org/10.1088/1402-4896/ac8a27
[62] Chapter 5 - Thermochemistry, in Practical Chemical Thermodynamics for Geoscientists, B. Fegley, Editor. 2013, Academic Press: Boston. p. 127-172; https://doi.org/10.1016/B978-0-12-251100-4.00005-5
[63] Wu, J., et al., Journal of Alloys and Compounds, 2017. **693**: p. 859-870; https://doi.org/10.1016/j.jallcom.2016.09.225
[64] Zoubir, M.H., et al., Revista Mexicana de Física, 2024. **70**(2 Mar-Apr): p. 020501 1–9-020501 1–9; https://doi.org/10.31349/RevMexFis.70.020501
[65] Khan, B., et al., Journal of Alloys and Compounds, 2015. **647**: p. 364-369; https://doi.org/10.1016/j.jallcom.2015.06.018
[66] Nguyen, D.K., J. Guerrero-Sanchez, D.M. Hoat, Physica E: Low-dimensional Systems and Nanostructures, 2024. **162**: p. 116003; https://doi.org/10.1016/j.physe.2024.116003
[67] Ishfaq, M., et al., Physica B: Condensed Matter, 2023. **664**: p. 415025; https://doi.org/10.1016/j.physb.2023.415025
[68] Murtaza, G., et al., Computational materials science, 2014. **85**: p. 402-408; http://dx.doi.org/10.1016/j.commatsci.2013.12.054
[69] Saleem, S., et al., Physica B: Condensed Matter, 2023. **667**: p. 415163; http://dx.doi.org/10.1016/j.physb.2023.415163
[70] Delice, S., et al., Journal of Physics and Chemistry of Solids, 2019. **131**: p. 22-26. https://doi.org/10.1016/j.jpcs.2019.03.004
[71] Potter, K.S., J.H. Simmons, Chapter 6 - Energy-related optical materials, in Optical Materials (Second Edition), K.S. Potter and J.H. Simmons, Editors. 2021, Elsevier. p. 309-368 https://doi.org/10.1016/B978-0-12-818642-8.00006-5
[72] Sudarsan, V., 8 - Optical Materials: Fundamentals and Applications, in Functional Materials, S. Banerjee and A.K. Tyagi, Editors. 2012, Elsevier: London. p. 285-322; https://doi.org/10.1016/B978-0-12-385142-0.00008-8
[73] Saleem, S., et al., Physica B: Condensed Matter, 2024. **692**: p. 416378; https://doi.org/10.1016/j.physb.2024.416378
[74] Benchehima, M., et al., Computational Materials Science, 2018. **155**: p. 224-234; https://doi.org/10.1016/j.commatsci.2018.08.050
[75] Benatmane, S., et al., Indian Journal of Physics, 2019. **93**: p. 627-638; http://dx.doi.org/10.1007/s12648-018-1333-y
[76] Bentayeb, A., et al., Journal of Computational Electronics, 2019. **18**(3): p. 791-801; https://link.springer.com/article/10.1007/s10825-019-01338-y

[77] Selmani, Y., et al., Physica B: Condensed Matter, 2022. **644**: p. 414204 https://doi.org/10.1016/j.physb.2022.414204
[78] Saleem, S., et al., Physica B: Condensed Matter, 2024. **692**: p. 416378; https://doi.org/10.1016/j.physb.2024.416378
[79] Batool, A., et al., Applied Surface Science Advances, 2022. **11**: p. 100275; https://doi.org/10.1016/j.apsadv.2022.100275
[80] Bhattacharjee, R., S. Chattopadhyaya, Solid State Sciences, 2017. **71**: p. 92-110; https://doi.org/10.1016/j.solidstatesciences.2017.06.010
[81] Shaukat, A., et al., Physica B: Condensed Matter, 2009. **404**(21): p. 3964-3972; https://doi.org/10.1016/j.physb.2009.07.147
[82] Hassan, M., et al., Materials Science and Engineering: B, 2018. **238**: p. 50-60; http://dx.doi.org/10.1016/j.mseb.2018.12.006
[83] Mal, I., et al., Materials Science in Semiconductor Processing, 2021. **121**: p. 105352; https://doi.org/10.1016/j.mssp.2020.105352
[84] Moussa, R., et al., Current Applied Physics, 2023. **55**: p. 82-92; https://doi.org/10.1016/j.cap.2023.09.004
[85] Gagui, S., et al., Journal of Molecular Modeling, 2020. **26**: p. 1-21; https://doi.org/10.1007/s00894-020-04370-z
[86] Tanveer, W., Mahmood, Q., Mahmood, I., Ashiq, M. G. B., Ramay, S. M., Mahmood, A. (2020); Chemical Physics, 532, 110690; https://doi.org/10.1016/j.chemphys.2020.110690